# On the optimum separation distance for minimum noise of contra-rotating rotors

P. Chaitanya*, P. Joseph, S. D. Prior, A. B. Parry

*University of Southampton, SO17 1BJ Southampton, UK.*

**Abstract**

Overlapping rotor systems are currently used on some urban flight vehicles and will become increasingly common in future electric propulsion, since they provide one of the most compact platform volumes per thrust. This paper presents the results of a detailed experimental investigation of co-axial contra-rotating rotor configuration at hover condition. A detailed parametric study is performed to investigate the sensitivity of radiated noise to axial separation distance. An optimum separation distance $z$ to rotor diameter $D$ of 0.25 has been identified, whereby minimum radiated noise is obtained. The reason for this optimum has been explored and the balance between various interaction noise sources in co-axial configuration is discussed in the paper. It is also shown that the minimum radiated noise was roughly found where the aerodynamic efficiency is maximum.

*Keywords:* Contra-rotating rotors, Optimum separation distance, Source balance, Potential field interactions, Tip vortex interactions.

## 1. Introduction

The global interest in small multi-rotor drones, Unmanned Aerial Vehicles (UAV's) and remotely piloted aircraft systems (RPAS) is growing rapidly. By 2023, the FAA now predicts there will be 835,000 commercial drones, which represents a tripling of their number over the next two years. It is now widely accepted that noise is one of the main factors that could limit the public acceptance and adoption of these systems [1].

Drones are currently designed for performance, with relatively little consideration given to noise. As the drone delivery market intensifies over the coming years, the payload requirement will inevitably increase by a factor of between 50 and 100, leading to further problems with public acceptance. One way to achieve this increase in payload capability is by the use of compact drone architectures, such as co-axial or overlapping rotors. As we shall show in this paper,

*Corresponding author

*Email address:* c.c.paruchuri@soton.ac.uk (P. Chaitanya*)

the noise from co-axial contra-rotating rotors is highly complex due to the potentially large number of aerodynamic sources that can exist due to the two rotors individually and their interaction. Moreover, each of these rotor-alone and interaction sources have tonal and broadband contributions. Whilst there has been some work on the prediction [2, 3, 4, 5, 6, 7, 8, 9, 10, 11, 12, 13, 14, 15, 16, 17, 18, 19, 20, 21] and measurement of individual tonal and broadband sources on co-axial contra-rotating rotors, there has been very limited work investigating the relative balance between these various noise contributions. This paper is a detailed experimental investigation into the balance of rotor-alone and interaction noise sources, with particular emphasis on the variation of the source balance with varying separation distance between rotors. This paper is restricted to co-axial contra-rotating configurations with zero net torque at hover.

*Aerodynamic studies*

Co-axial contra-rotating rotors suffer from losses in aerodynamic performance due to the interactions of the downstream rotor operating in the wake of the upstream rotor. To maximise efficiency, therefore, the rotors are separated at the optimum distance at which the wake of the downstream rotor will be coincident with that of the contracted upstream rotor wake. A comprehensive review of the early research related to the aerodynamic performance of co-axial contra-rotating rotors, their wake characteristics, and methods of performance analysis has been presented by Ref. [22]. Important contributions to the measurement and analysis of the performance of co-axial rotor configurations were carried out by Ref. [23] and co-workers during the late 1970s and early 1980s. They proposed that co-axial contra-rotating rotors performance could be optimised with an appropriate selection of rotor parameters, such as blade pitch and separation distance, which would lead to an improvement in performance compared to a single rotor delivering the same thrust. An optimum pitch angle combination between upstream and downstream rotors was identified for a given rotor separation distance.

Much later Leishman and Syal [24] applied momentum theory in an attempt to development of appropriate figure of merit expressions for a co-axial contra-rotating rotor system. The maximum efficiency of the co-axial rotor system was shown to occur at the rotor separation distance at which the downstream rotor operates in the fully developed slipstream of the upstream rotor. In a different experimental study, Lei et al. [25] performed a sensitivity study into the effect of separation distance on aerodynamic performance on a co-axial rotor system. The performance was measured for seven rotor separation distances $z$ varying from $z/D$=0.16 to 0.38, where $D$ is the rotor diameter. The best aerodynamic performance was found to occur at the separation distance of $z/D$=0.19, which was attributed to the minimum aerodynamic interactions between the top and bottom rotor. No comparison with the theoretical prediction was provided.

Brazinskas et al. [26] performed a systematic parametric study on aerodynamic performance due to the effect of rotor separation distance. They demonstrated that for distance greater than $z/D$ equal to 0.25 there is no signifi-

cant effect on the overall aerodynamic performance. Co-axial contra-rotating rotors were found to give a 4% improvement in rotor efficiency compared to co-rotating configurations, which they attributed to the effects of swirl. Other studies on the aerodynamic performance of co-axial rotors such as Ref. [27, 28] have found that, for the same combined thrust, the thrust from the downstream rotor increases while the thrust from the upstream decreases as the separation distance is reduced. Furthermore, the overall performance of the co-axial contra-rotating rotors was found to be independent of the separation distance for $z/D > 0.15$. More detailed investigations into the aerodynamic characteristics of contra-rotating rotors have been performed by Ref. [29, 30] who demonstrated that the performance depends on the various vortex-vortex, vortex-vortex sheet interactions between the rotors, which was found to affect the spatial and temporal characteristics of the structure of the wake from the upstream rotor, and hence affect overall aerodynamic performance. All the previous aerodynamic studies are performed on wide range of applications from Helicopters to small drones. However, the effect of the Reynolds number is not fully understood.

*Aeroacoustics studies*

The previous research on the aerodynamics of contra-rotating rotors has highlighted the rotor separation distance as being one of the key parameters in the design of small-scale co-axial contra-rotating rotors. However, no comparable studies have been performed on the effect of separation distance on their acoustic characteristics. All previous acoustic measurements on contra-rotating rotors were confined to very large co-axial Contra Rotating Open Rotors (CRORS) for use on civil aircraft [31, 32, 33, 34, 35, 36].

Woodward [33] performed a detailed parametric study on the measured noise radiation from a high speed advanced contra-rotating rotor in the 9-by 15-Foot Anechoic Wind Tunnel at the NASA Lewis Research Center. The rotor was operated over range of blade pitch settings, tip speeds and the three rotor separation distances of $z/D$ =0.1371, 0.1710 and 0.2419. They found that at the cruise condition, where the axial Mach number equals 0.8, increasing the rotor separation was found to reduce tonal noise due to interaction between the rotors by up to 7 dB, while rotor-alone tones showed little sensitivity to rotor spacing. However, at the slightly lower axial Mach numbers of 0.72 and 0.76, another study performed on the same rig, Dittmar [34], the noise was found to increase as the rotor separation distance was increased, contrary to the behaviors observed at $M = 0.8$. A possible explanation for this behaviour was attributed to the interaction of the tip vortex with the downstream rotor. At the lower axial Mach numbers, it was speculated that the area over which the tip vortex interacts with the downstream rotor increases as the tip vortex grows due to increasing separation distance, causing an increase in noise. By contrast, at the higher Mach number of 0.8, the tip vortex misses the downstream rotor as it convects downstream.

In an attempt to reduce the noise due to tip vortex interaction, Dittmar et al. [37] investigated the benefits of cropping of the downstream rotor. In a CROR with upstream and downstream rotor diameter of 0.620 m and 0.607 m

the downstream rotor was cropped to 0.537 m ( 10%), resulting in overall noise reductions of 3 dB. The noise reduction was attributed to reductions in the interaction 'tones' occurring at the sum and difference frequencies $\omega_{mn} = m\Omega^{+}+n\Omega^{-}$ and the tones occurring at the downstream rotor harmonics $m\Omega^{-}$ due to tip vortex interaction. This mechanism is explored in greater detail in Section 7 and 8 below. [35] performed an exhaustive study into the effects on aerodynamic and aeroacoustic performance due to rotor separation distance, blade numbers, angle-of-attack, pylon proximity, mismatched rotor speeds, and the effect of cropping. Two different rotor separation distances of $z/D$ of 0.17 and 0.24 were investigated with and without cropping of the downstream rotor. Enhanced noise reductions of up to 5.5 EPNdB (Effective perceived noise in decibels) were observed with increasing rotor separation distance for the case of the downstream cropped rotor compared to a 1.5 dB EPNdB without cropping. The reason for this enhanced reduction in the interaction tones was again attributed to the prevention of the tip vortex from interacting with the downstream rotor and also due to an increased decay of the upstream blade wakes with increased rotor spacing.

Recently, McKay et al. [38] performed an experimental investigation of effect on the noise of a single stationary contra-rotating rotor due to variations in rotor diameter, rotor spacing, and blade numbers. They observed that interaction tones were about 20 dB higher than rotor alone tones. However, their investigation was limited to only two separation distances and therefore clear optimum spacing could not be identified.

With the exception of the recent work of McKay et al. [38, 39, 40], all the previous work surveyed above was performed on high speed co-axial Contra Rotating Open Rotors (CRORS). The balance between the different noise sources are likely to be very different for typical rotors on drones whose chord-based Reynolds number ($< 10^5$) will be significantly lower. Moreover, apart from the previous work on CRORs no other work has appeared in the open literature on the balance between the various noise sources and their variation with separation distance for the purpose of identifying the optimum low-noise rotor separation distance. Psychoacoustic analysis of contra-rotating rotor on the current paper data is presented in Ref. [40]. Based on psychoacoustic metrics, the optimal rotor axial separation distance $z$ to rotor diameter $D$ is identified between 0.2 to 0.4. However, physical insights and the reason behind the optimum separation distance between the rotor are not investigated in Ref. [40].

The current paper presents the results of a detailed experimental investigation into the breakdown of the different noise sources on a small-scale contra-rotating fan and its sensitivity to the rotor axial separation distance. The range of rotor diameters considered in the study are 14-18 inch and range of Tip Mach numbers investigated in the present study are 0.2. It will be shown in the paper that the separation distance for which the radiated is a minimum noise occurs at the optimum separation distance $z/D = 0.25$, which is observed closely to the distance of maximum aerodynamic efficiency, roughly consistent with the previous work cited above. The balance of sources and the reasons for this optimum separation distance will be investigated in this paper.

Section 2 deals with an overview of the dominant noise generation mechanisms on two contra-rotating co-axial rotors. Section 3 describes the experimental setup and experimental procedure. Section 4 is the main section in this paper and describes the acoustic measurements, where a clear optimum separation distance is identified. This section also provides a breakdown of the dominant noise sources. Section five provides a characterisation of the unsteady velocities downstream of the upper rotor in an attempt to characteristic the flow impinging upon the lower rotor. Section 6 provides an overview of the time-space variation in velocity in attempt to understand the noise generation mechanisms. Section 7 is the first section dealing with individual sources and is concerned with the role of the tip vortex on broadband noise. Similarly, section 8 examines the influence of separation distance on the tonal noise. Section 9 examines the effect of rotor dimeter mismatch on the radiated noise. Finally, aerodynamic performance is discussed in section 10 followed by some conclusions in section 11.

## 2. A review of dominant noise generating mechanisms in contra-rotating rotors

The noise radiation mechanisms due to two closely coupled rotors is complex owing to the potentially large number of distinct self-noise and interacting sources that may be present, as identified in figure 1. The noise source in this figure at the hover condition can be categorised into three broad categories: 1) Rotor self-noise, 2) Rotor installation noise, 3) Rotor-Rotor interaction noise. This paper will lay particular emphasis on 3) which we shall show below is the dominant source for contra-rotating rotors.

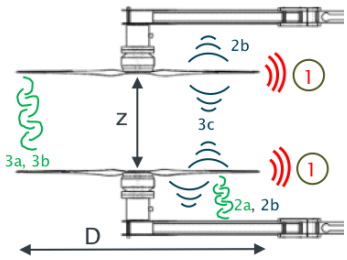


Figure 1: Dominant sources of noise for contra-rotating rotor system

Each of these categories themselves comprise a number of complex source mechanisms. The primary dominant rotor self-noise sources have been summarised in Ref. [41] and are: (1) tonal self-noise, which is generated by the volume displacement and steady aerodynamic blade loading; (2) blade-vortex interaction (BVI), which occurs when the blade tip vortex impinges on a subsequent blade; (3) blade-wake interaction (BWI), which occurs when the turbulent wake formed by one blade impinges on a subsequent blade; and (4) Turbulent boundary layer-trailing edge self-noise, which is due to the turbulent boundary layer interacting with the trailing edge. For a rotor operating in an otherwise low-turbulence mean flow, of these various sources the tonal components due to steady blade loading and aerofoil thickness are usually dominant, while the broadband noise component is relatively weak. In addition, there are quadrupole noise sources at high speeds.

Another important noise source from a single-rotating rotor is its interaction with any adjacent booms that may be present. A recent study by NASA has shown that rotor self-noise can be increased by up to 25 dB by introducing a small boom in close proximity to the rotor [42]. This tonal and broadband noise source is generated when the wake and the potential near field from the rotor interacts with the boom (See 2a and 2b in Fig. 1). We have performed a parametric study on the noise due to rotor-boom interaction and observed that the potential field interactions are dominant when boom is much closer to the rotor (d/D<0.2), where d is the distance between the rotor and boom Hence, the boom is placed at d/D=0.2 from the rotor. The rotor self-noise therefore only includes rotor alone tones and broadband noise, with only a small contribution arising from the noise due to boom-wake-rotor interaction and rotor-wake-boom interactions. Similarly, Rotor-Rotor interaction noise occurs when the spiralling wake and tip vortex from the upstream rotor interact with the downstream rotor rotating in the opposite direction (See 3a and 3b in Fig. 1). In addition, in this paper we shall show that periodic chopping of the large-scale tip vortices will generate pseudo tones from the downstream rotor [6], which becomes the dominant noise source, especially at sufficiently large separation distances. At sufficiently small separation distances, we will further show in this paper that the dominant source of noise is the tones arising from the interaction of the potential field of each rotor with the adjacent rotor (See 3c in Fig. 1). Finally, this paper will demonstrate that the optimum separation distance for minimum noise occurs when these sources are roughly equal.

## 3. Experimental set-up and procedure

### *3.1. Contra-rotating rotor rig*

The experimental investigation into the balance of noise sources and their sensitivity to separation distance was performed on a contra-rotating fan rig, typical of a mid-size drone (16 inch), corresponding to blade-chord based Reynolds number of $2 \times 10^5$. The rotors were powered by two FOXTECH W61-35 brushless DC (BLDC) (16 poles) 700 W motors mounted on a carbon fibre beam as shown in figure 2a, which allows for maximum rotor speeds of 5000 RPM, a maximum thrust of 40 N for the largest diameter rotor. Three commercially available T-Motor rotors with diameters of 14 inch, 16 inch and 18 inch were investigated. The rotor blade geometry was optimised for use in isolated propulsion systems and for specific use in contra-rotating systems. Two Hyperion HP-EM2-TACHBL sensors were used to measure the precise rotational speed (Rotations Per Minute, RPM) of the rotors. Two Maytech 40A-OPTO speed controllers were used to accurately control the BLDC motors. Varying rotor separation distance between $z/D$ between 0.05 and 1 was achieved by the use of a custom linear actuator which allows the continuous traverse of the upstream rotor with respect to a fixed downstream rotor. A detailed description of the rig is presented in Ref. [26].

In the study presented in this paper, alongside the acoustic measurements were detailed measurements of the fan rig's aerodynamic performance, such as

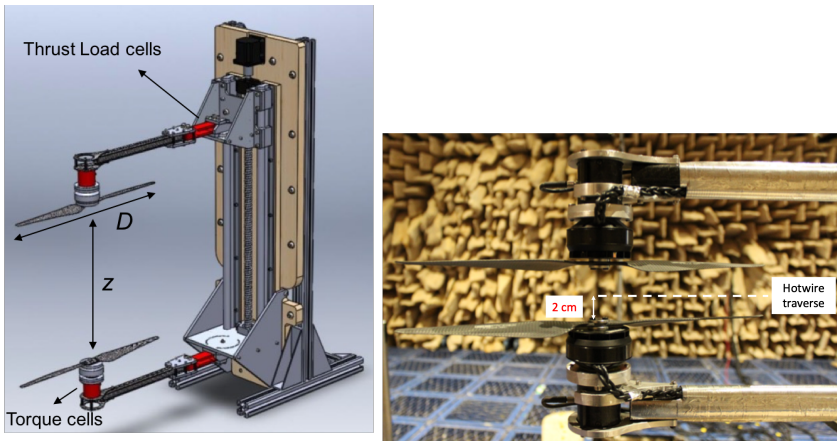


Figure 2: a) Test-rig side view showing the maximum axial rotor separation [26] b) Photograph of overlapping rig inside the ISVR anechoic chamber.

thrust, torque and input electrical power to understand the relationship between noise radiation and efficiency. Two Zemic L6D shear load cells of capacity of 98 N (10 kg) located at the ends of both the arms of the test rig were used to measure the individual thrust of each rotor, as shown in figure 2a. RTS-100 reaction torque sensors were mounted underneath each rotor to adjust torque in order to maintain zero net torque. The sensor data-gathering and test rig control system are fully automated and achieved using National Instrument's Labview and Phidgets modules [26]. Both voltage and current are measured simultaneously to calculate the overall efficiency of the multi-rotor propulsion system. Two Allegro ACS712T Hall Effect type 30 A current sensors using Phidget 1122 breakout boards were used to measure individual BLDC motor currents, while a National Instruments NI 9215 module was used to directly measured the voltage.

### *3.2. Far-field noise and aerodynamic measurements*

Far-field noise measurements on the contra-rotating rig were carried out in the anechoic chamber at the Institute of Sound and Vibration Research with dimensions of 8 m x 8 m x 8 m as shown in figure 2b. The walls are acoustically treated with glass wool wedges whose cut-off frequency is 80 Hz.

Far-field noise measurements were made using 10, half-inch condenser microphones (B&K type 4189) located at a constant radial distance of 2.5 m from the centre of the fan rig. These microphones are placed at emission angles ranging between 0° and 85° measured relative to the rotor axis. Note that the microphone at 0° emission angle is located upstream of the upper rotor. Measurements were carried for 10 s duration at a sampling frequency of 50 kHz, and the noise spectra were calculated with a window size of 1024 data points corresponding to a frequency resolution of 48.83 Hz and a Bandwidth-Time ($BT$) product of about 500, which is sufficient to ensure negligible variance in the

spectral estimated with this frequency resolution.

The acoustic pressure at the microphones were recorded at different combined trust settings varying from 2 to 20 N in steps of 2 N for 16 separation distances ($z/D$) varying from 0.05 to 1. The noise from each rotor in isolation was also measured for value of thrust between 1 to 10 N in steps of 1 N. Sound Power Level spectra $PWL(\omega) = 10\log_{10}(S_w(\omega)/W_{ref})$ were calculated by integrating the Power Spectral Density (PSD) of the acoustic pressure over the 10 microphones using the equation 1,

$$S_w(\omega) = \sum_{i=1}^{i=N-1} \frac{[S_{PP}(\omega,\theta_i) + S_{PP}(\omega,\theta_{i+1})]\,\pi R^2 \cos(\theta)\Delta\theta_i}{\rho c} \tag{1}$$

where $S_w(\omega)$ is the spectral density of the sound power radiated between the radiation angles $[0° - 85°]$, $W_{ref} = 10^{-12}$ W and $S_{pp}(\omega,\theta_i)$ is the acoustic pressure PSD (Power Spectral Density) measured at angle $\theta_i$ with respect to rotor plane and $N$ is the number of microphones, $R$ is the radius of the microphone array, $\Delta\theta$ is the angle between two adjacent microphones, $\rho$ is the density of the ambient air, and $c$ is the speed of sound.

The rotors are placed around 1.5 m above the ground to avoid recirculation in the presence of ground. A time-frequency analysis is also performed to investigate the influence of recirculation on the radiated noise. A very small differences are observed due to re-circulation. The noise measurements are insensitive to the positioning of the rig suggesting that the re-circulation is not a significant effect on the radiated noise.

A thin layer of absorbing material has been used on the structure to minimise sound reflections without significantly effecting aerodynamic performance. However, a thicker layer is tried but this enhanced the noise as the surface is moved closer to the rotor. Hence, a parametric study is performed to identify an optimum foam of 20 mm thick is used to avoid sound reflections. The measurement plane is perpendicular to the setup to avoid any additional noise.

Measurements of the steady and unsteady velocity between the two rotors was carried out using Hot-wire anemometer (TSI IFA-300 CTA) to understand the flow characteristics impinging on the downstream rotor due to rotating upstream rotor. The hot wire probe was traversed along 20 radial locations, 2 cm above the downstream rotor for 16 separation distances $z/D$ at the two combined thrust conditions of 10N and 16N. The single hot-wire probe was oriented horizontally and was therefore sensitive to flow arriving in the vertical plane.

## 4. Acoustic performance

### *4.1. Typical noise spectral characteristics*

Before investigating the source breakdown for the contra-rotating fan rig we first present a typical sound power spectrum in order to illustrate its general

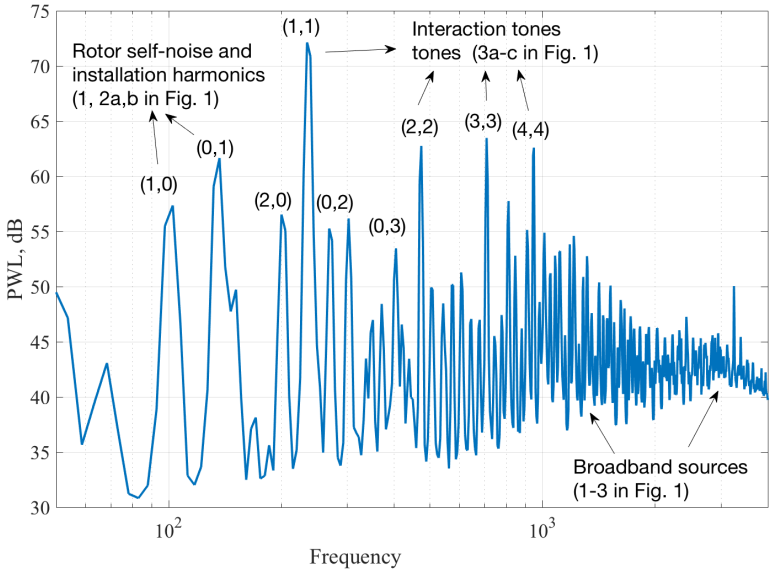


Figure 3: A typical sound power levels spectrum for contra-rotating rotors at a separation distance of $z/D = 0.1$ and combined thrust of 16 N.

character and complexity. Figure 3 shows a typical sound power level spectrum for the contra-rotating fan rig, with the upstream and downstream rotors operating at the two different RPMs of 2960 and 4084 respectively, at a separation distance of $z/D = 0.1$ and combined thrust of 16N. These tones can related to rotor alone tones at the blade passing frequencies of individual rotors $\omega_{m,0} = mB^+\Omega^+$ and $\omega_{0,n} = nB^-\Omega^-$ and also the sum and difference interaction tones at frequencies $\omega_{m,n} = m\Omega^+ + n\Omega^-$. These frequencies $(m, n)$ are indicated for some of the dominant tones. The dominant noise sources in relation to figure 1 are also indicated in this figure. The spectrum is dominated by tones especially below 1000Hz ($\approx 10^{th}$ harmonic) and by broadband noise at frequencies above about 2000Hz. It is clear that the interaction tones are dominant over the rotor alone tones for this configuration, which we shall show below includes contributions from the rotor potential fields, tip vortex interaction and wake rotor interactions. This paper seeks to identify the relative importance of each these individual component sources at different operating conditions and relative separation distances between the rotors, for the purpose of identifying an optimum separation distance for minimum radiated noise. The reason behind this optimum distance is explored.

### *4.2. Optimum separation distance*

We now present the variation in the overall sound power level versus the rotor axial separation distance $z/D$ for 16" diameter rotors. We note that in

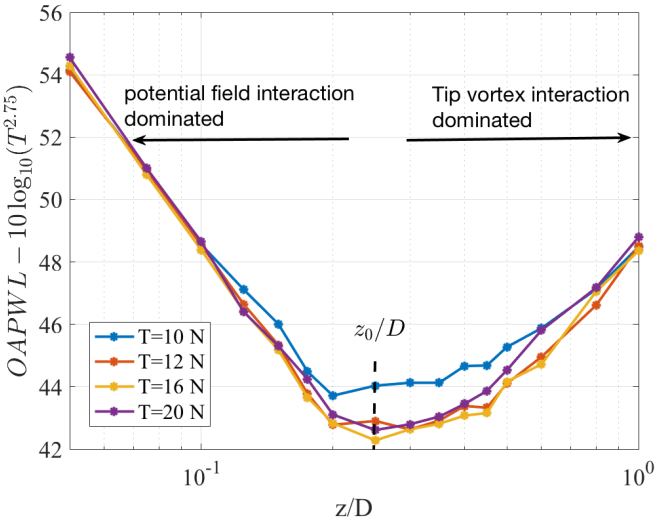


Figure 4: Overall sound power level variation with separation distance at various combine total thrust for 16" diameter rotor.

this case the net torque has been maintained at zero and hence the RPMs of identical rotors are almost identical $\Omega^+ \approx \Omega^-$, resulting in an unequal thrust distribution $T^+$ and $T^-$ between the two rotors. The overall sound power levels are calculated by integrating the power over the frequency range encompassing the first 40 harmonics of blade passing frequency. Figure 4 shows the overall sound power level plotted against non-dimensional separation distance $z/D$ varying from 0.05 to 1 for four different total thrust settings $T = T^+ + T^-$ of 10, 12, 16 and 20 N. The sound power levels have been scaled by $T^{2.75}$, which can be seen to provide excellent collapse of the overall noise data for the four thrust settings, particularly at values of $z/D < 0.5$. The collapse of the noise reduction values when appropriately scaled is better than 1 dB. This scaling of the noise with $T$ is well established for single rotors, and arises from the well known observation that fan noise varies as rotational velocity as $U^{5.5}$ and that thrust $T$ varies with velocity as $T \propto U^2$. Figure 4 indicates that this scaling is also valid for contra-rotating rotors where the basic aerofoil noise generation mechanisms are fundamentally the same.

Further insights into the scaling of the radiated sound power with rotation RPM $N$ and rotor diameter $D$ may be obtained by following the dimensional analysis presented in [43] for single rotors. [43] suggested that the radiated sound power $P$ is a function of the rotor mechanical power $P_i$, the blade tip Mach number $M_t$ and chord-based Reynolds number $Re_c$. Assuming identical upstream and downstream rotational speeds $N$ and diameters $D$, the radiated acoustic power may be related to the available mechanical by the non-dimensional functions $f$ and $g$ as,

$$\frac{P}{P_i} \propto f(M_t)g(Re_c) \tag{2}$$

The mechanical power imparted to the rotor is well known to be proportional to $N^3D^5$ and therefore,

$$\frac{P}{N^3D^5} \propto (ND)^a(ND^2)^b \tag{3}$$

The effects of Reynolds number on the acoustic efficiency $P/P_i$ are more difficult to identify. Cory [43] argues that the index $b$ should varying in the range of $0 > b > -1$ depending on the degree of flow separation on the blades. Here we adopt the average value of $b = -0.5$ and, assuming the blades radiate as aerodynamic dipole sources suggests a value of $a$=3. Combining these power laws, Cory [43] argues that for a single rotor, the radiated acoustic power varies as P$\propto N^{5.5}D^7$. The total noise therefore follows a thrust scaling law of $T^{2.75}$ and velocity scaling law of $U^{5.5}$, which is identical to the scaling law characteristics of aerofoil leading edge noise [44].

The second key results from the figure 4 is the clear existence of an optimum separation distance at $z/D = 0.25$ at which minimum radiated overall sound power level occurs. This figure suggests this optimum distance is almost independent of thrust and particularly well defined for the largest thrust setting at which the radiated noise is greatest. The reason behind this optimum separation distance will be shown in Section 8 below to be due to the balance between potential field interactions and tip vortex interactions.

The validity of the optimum separation distance observed for 16" rotor diameter is now extended for a smaller and larger rotor diameter. Figure 5 shows the overall sound power levels plotted against non-dimensional separation distance $z/D$ for all three different rotor diameters of 14", 16" and 18". Note that in order to maintain a constant combined thrust of 16 N in each case, the rotor speeds were adjusted appropriately. This figure reveals two important features. The first is a consistent value for the optimum separation distance $z_0/D$ for the three rotor diameters of about 0.25. Secondly, the overall sound power level is observed to reduce as the rotor diameter is increased while maintaining constant overall thrust. To maintain constant thrust when increasing rotor diameters from 14" to 18", the rotor RPM was reduced from 5117 to 3201 RPM. According to the scaling law $N^{5.5}D^7$, this change in $N$ and $D$ should provide an overall noise reduction of 3.5 dB. This prediction is roughly consistent with the results in figure 5, suggesting that larger diameter rotors operating at a lower RPM are quieter. The data for rotor with the mid-size diameter can be seen to deviate slightly from this scaling law, which may be attributed to the onset of additional sources, possibly due to flow separation at some radial locations along the blade. Also, note that the optimum distance doesn't change for dBA weighted noise data.

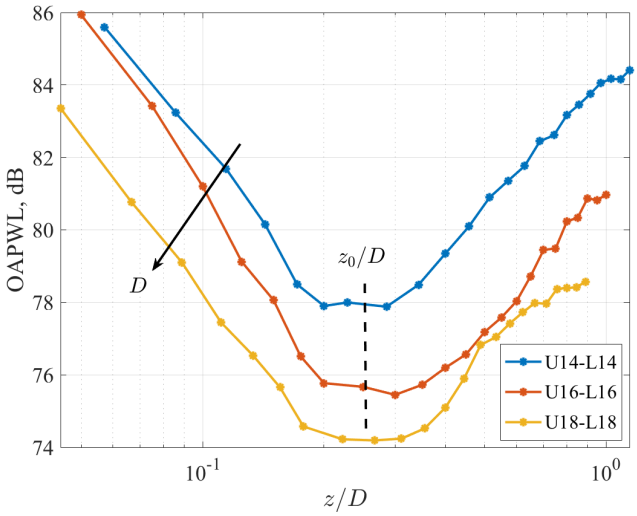


Figure 5: Overall sound power level variation with separation distance for various rotor diameters combinations at a fixed combined thrust of 16N. In the legend $U$ represented Upper rotor diameter and $L$ represented lower rotor diameter.

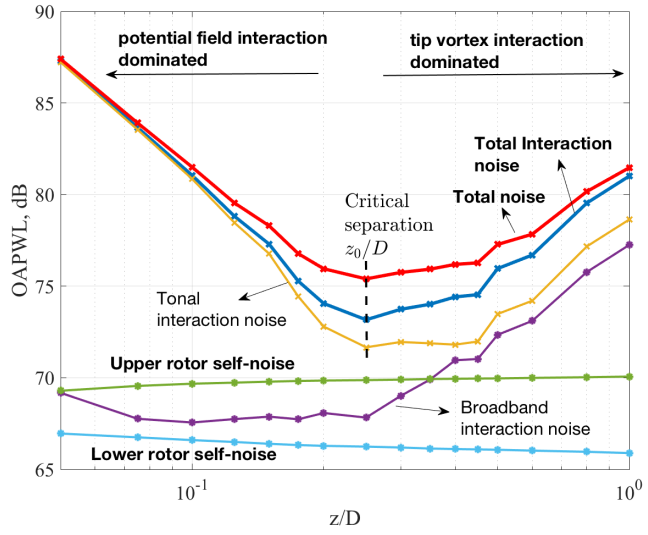


Figure 6: Overall sound power level variation for various sources with separation distance at a fixed combined thrust of 16N.

### *4.3. Source breakdown*

In this section we attempt to decompose the total overall radiated noise into the various dominant constituent noise sources discussed in Section 2. For counter-rotating rotors these sources can be broadly classified into rotor-self noise and rotor interaction noise sources. In the current study we include the noise due to the interaction with the adjacent boom as a rotor self-noise source since we are unable to separate this contribution from overall self-noise in the current rig. Rotor self-noise for the upstream and downstream rotors was measured separately with the adjacent rotor stationary. To ensure compatibility with the contra-rotating case, the thrust of each rotor was adjusted to be identical to that when operating in the contra-rotating configuration at every separation distance.

Figure 6 shows a comparison of the overall sound power levels plotted against $z/D$ at a fixed thrust setting of 16N for the two rotors operating simultaneously and at respective thrust individually. Also shown is the interaction noise obtained by subtracting the sum of rotor self-noise due to the upstream and downstream rotors from the total overall noise. The overall interaction noise has been further decomposed into its tonal and broadband noise contributions. The broadband component was isolated from the overall noise spectrum by applying a median filter whereby the spectrum at each frequency point is replaced by its median value from 10 points either side.

From this figure we can make the following key observations:

1. A clear optimum separation distance $z_0/D$ exists for minimum noise.
2. Interaction noise is dominant at all separation distances.
3. The sum of the rotor self-noise from the two rotors (not shown in the figure) is unimportant for most separation distances except close to the optimum separation distance where it is less than 3 dB of the overall noise. Thus, at the optimum distance there appears to be an equal contribution to the overall noise from self-noise sources and interaction noise sources.
4. Tonal noise contributions are dominant at separation distances of $z/D < 0.25$, which we shall show in the next section is due to the interaction of the rotor potential field with the adjacent rotor.
5. At separation distances $z/D > 0.25$ the tonal and broadband noise contributions are within 1 dB of each other. We shall show in Section 7 that the increase in broadband noise is due to enhanced turbulence impinging on to downstream rotor at larger separation distances. We shall also show in Section 8.2 that the dominant 'tones' at these large separation distances are pseudo-tones arising from the periodic chopping of the blade tip vortex from the upstream rotor.

The main reason for the differences in radiated noise between upper and lower rotor is due to difference in thrust between upper and lower rotor. The upper rotor is driven to generates higher thrust to maintain zero net- torque. The thrust from the lower rotor is reduced due to wake interactions from the upper rotor. However, there will be a small contribution to interaction tones

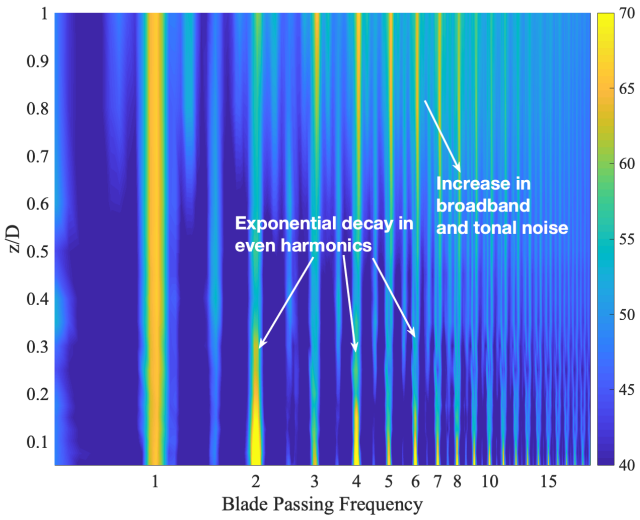


Figure 7: Sound power level color maps plotted against non-dimensional distance $z/D$ and blade passing frequency at a fixed combined thrust of 16 N.

due to the wake of the upper boom interacting with the upper rotor,. The figure below, show the radiated overall sound power level vs thrust for both rotors, demonstrating a small difference in the radiated noise due to the upper rotor resulting from enhanced boom-rotor interactions. The main reason for the difference in the noise due to upper and lower rotor self-noise in Fig. 6 is therefore due to differences in thrust rather than wake-rotor interactions. The difference in the thrust is the result of performing all these measurements sat zero net torque.

To understand in greater detail the effect of rotor separation distance on noise at a fixed combined thrust of 16 N, the total radiated sound power spectrum is plotted against $z/D$ and frequency normalised on the Blade passing frequency in Figure 7. The blade passing frequency tones are clearly observed. Note that both rotors have almost identical RPM in this case as the net torque is set to zero and hence the blade passing frequencies from both rotors are almost identical. A clear decay in sound power level at even harmonics of blade passing frequency is observed for $z/D < 0.25$. This is attributed to decay in potential field interactions which will be shown in Section 8.

For larger separation distances $z/D > 0.25$, figure 7 indicates that both tones and broadband noise begin to increase as the separation distance is increased. The reason for this behaviour will be shown below due to the tip vortex from the upstream rotor interacting with the downstream rotor. The reason for the increase is explained with detailed hot-wire measurements shown in next Section 5.

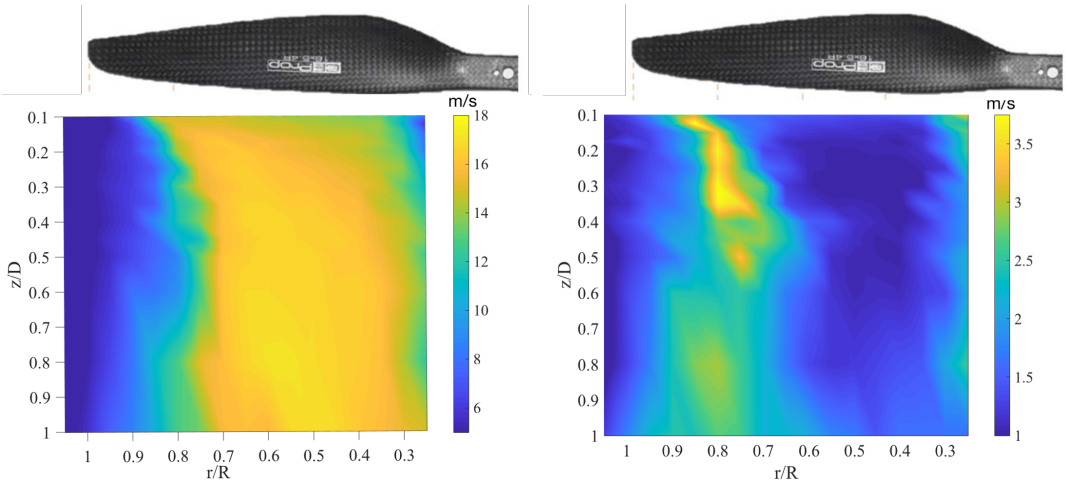


Figure 8: Mean velocity (left) and rms (right) color maps plotted against the normalised separation distance $z/D$ and normalised radius $r/R$ for a 16" rotor diameter at fixed thrust of 10 N.

## 5. Characteristics of unsteady velocity impinging on the downstream rotor

This section presents hot-wire measurements performed 2 cm above the downstream rotor for varying rotor separation distances, and aimed at characterising the unsteady velocity impinging on the downstream rotor. The measurements were made to understand the reasons for the increase in noise associated with increasing separation distance ($z/D > 0.25$). Figure 8a and b show the mean velocity and RMS velocity color maps plotted against $z/D$ and normalised radius $r/R$ at a fixed combined thrust of 10 N. These quantities were deduced from the average of the hot wire signal measured over 20 s and therefore represent the circumstantially averaged mean flow and turbulence values respectively. Clear 'S-boundary' type flow behaviour can be observed in the mean flow variation, which is consistent with momentum theory discussed in previous aerodynamic studies [29, 30] on tip vortex evolution. Also shown in the RMS velocity color maps is a strong tip vortex evolution near the tip. Depending on the separation distance, the radial location at which the tip vortex interacts with the downstream rotor decreases, eventually becoming constant and tending towards a value of approximately $0.75R$ for separation distances $z/D > 0.4$. This behaviour can be readily predicted from simple momentum theory where the mean velocity in the far wake region is predicted to double while the area is predicted to halve, resulting in a reduction in radius by a factor of $1/\sqrt{2}$.

We now focus on the characteristics of the unsteady flow at the optimum separation distance $z_0/D = 0.25$ and a single separation distance greater than the optimum $z_0/D = 0.8$ aimed at explaining the noise increase due to tip vortex

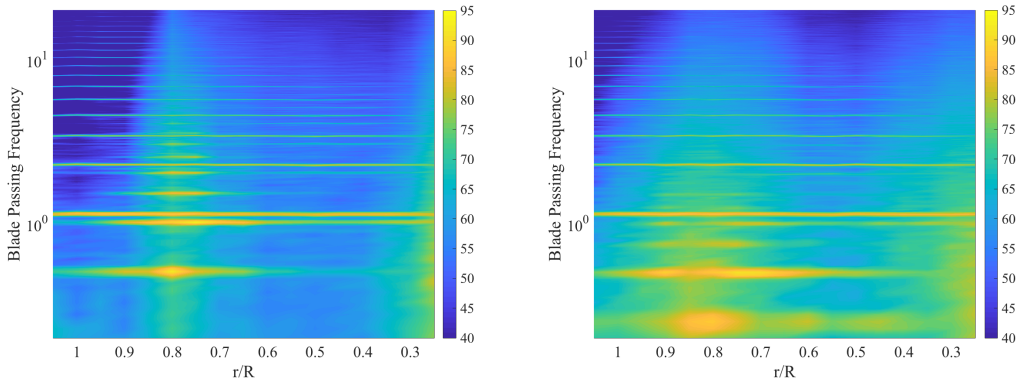


Figure 9: PSD of velocity contours in dB plotted against normalized radius $r/R$ and Blade passing frequency at a fixed separation distance of $z/D = 0.25$ (left) and $z/D = 0.8$ (right)

interactions. Figures 9a and b show the PSD of the circumstantially averaged unsteady velocity color maps plotted against Blade passing frequency (BPF) and radius $r/R$ for the two different separation distances. This figure reveals two important observations. First, the unsteady velocity 2 cm above the downstream rotor is significantly greater at the tip region $r/R \approx 0.8$ compared with the in-board regions due to the turbulent wake from the upstream rotor. As the separation distance is increased, the PSD at low frequencies (<1BPF) becomes significantly increased compared to the levels at the optimum separation distance of $z/D = 0.25$. The second observation is the increase in the radial extent of the tip vortex with the increase in separation distance. This behaviour has been previously observed by Ref. [45]. We also observe significant RMS velocity levels at sub-harmonic frequencies of BPF at large separation distances. The reasons for this behaviour is discussed below.

One of the most important features of figure 6 is the increase in broadband noise as the axial separation distance is increased beyond the optimum distance. In an attempt to explain this behaviour the unsteady velocity PSD plotted in figure 9 is integrated over the radius weighted by the cube of the mean flow speed onto the downstream rotor according to,

$$\int_{r_{hub}}^{r_{tip}} U(r)^3 S_{uu}(\omega, r) \mathrm{d}r. \tag{4}$$

This velocity weighting of the turbulence provides a simple measure of the total acoustically-weighted turbulence velocity spectrum. The velocity weighting $U^3$ appears explicitly in the expression for the far-field PSD for leading edge noise and accounts for the acoustic response of the blade at mean flow speed $U$ [46]. The results of this integration are plotted in figure 10 for varying separation distance $z/D$ of 0.1 to 1, against frequency normalised on BPF of the downstream rotor.

Figure 10 shows that the velocity amplitude of the tones $(m, 0)$ associated

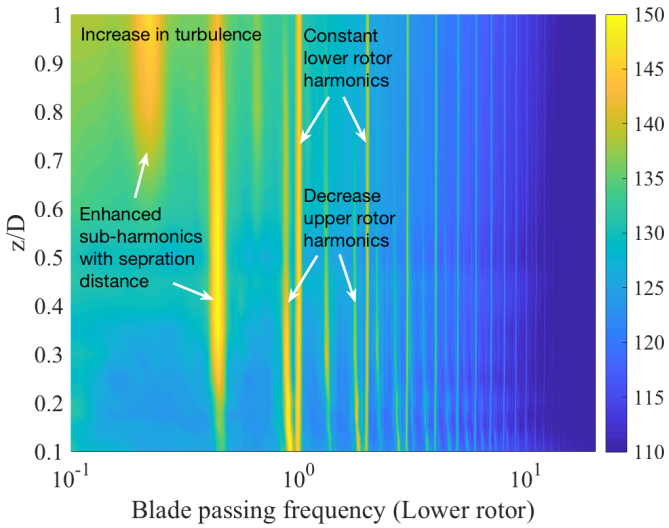


Figure 10: PSD of unsteady velocity color maps in dB integrated over radius with $U^3$ weighting plotted against blade passing frequency and separation distance at a fixed combined thrust of 10 N.

with the upstream rotor vary with increasing $z/D$ while the amplitudes for the downstream rotor tones $(0, n)$ are independent of separation distance since they are associated with its potential field and is therefore unrelated to $z/D$. The velocity amplitudes due to the upstream rotor $(m, 0)$ are observed to decrease with increasing separation distance with the notable exception of the tone at 0.5 BPF (0.5,0), which we discuss below.

The largest increase in broadband spectral content is observed in the low frequency range significantly below 1BPF. The cause of sub-harmonic frequencies can partly understood by plotting the variation in standard deviation of the velocity obtained from the tip vortex as a function of blade angle $\tilde{\theta}$ as observed in the reference frame rotating with the upstream rotor. This was achieved by relating the blade angle $\theta$ at any instant in time $t$ by $\theta = \Omega t$, by the use of a tachometer signal from the upstream rotor. The hot wire signal was adaptively resampled to ensure that there was precisely the same number of data samples for each blade rotation to allow averaging of the mean and rms velocity over many rotations. Following resampling of the measured velocity signal $u(t)$ at a given position $z$ and $r$ was decomposed into the sum of the coherent average $\overline{U}(\tilde{\theta})$ plus a fluctuating random component corresponding to the turbulent velocity fluctuations $u_\sigma(\tilde{\theta})$. The time varying velocity signal was ensemble-averaged over a period of rotation $T$ for a duration of 20 s according to,

$$\overline{U}(\tilde{\theta}) = E\{u(\tilde{\theta})\} = \lim_{K\to\infty} \frac{1}{K} \sum_{K=0}^{K} u(\tilde{\theta} + 2\pi k) \tag{5}$$

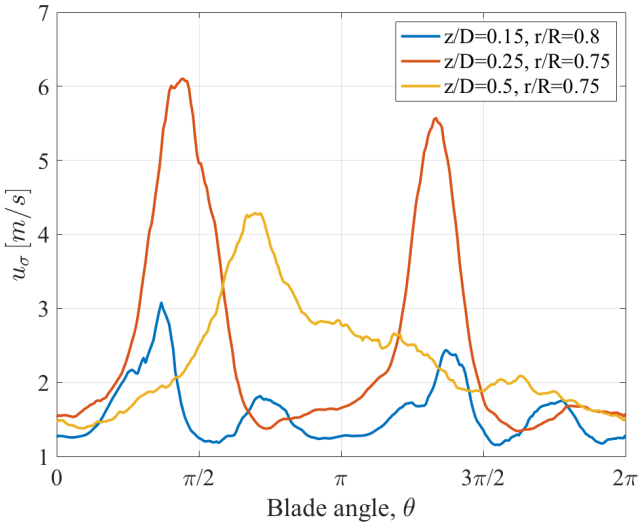


Figure 11: Standard deviation of the measured velocity at three different separation distances of $z/D$=0.15, 0.25 and 0.5 at fixed upstream rotor thrust.

where $K$ is the number of rotations $k = 20/T$, where precise values of $T$ for each rotation were obtained from the tacho signal sampled at 20 kHz.

Similarly, the $\tilde{\theta}$-variation of the velocity variance $u^2_\sigma(\theta)$ is given by,

$$u^2_\sigma(\tilde{\theta}) = E\{u^2(\tilde{\theta})\} = \lim_{K\to\infty} \frac{1}{K} \sum_{K=0}^{K} (u(\tilde{\theta} + 2\pi k) - \overline{U}(\tilde{\theta}))^2 \tag{6}$$

Figure 11 shows the standard deviation $u_\sigma(\tilde{\theta})$ of the measured velocity signal at three different separation distances of $z/D$=0.15, 0.25 and 0.5 at the radial positions of $r/R$=0.8 and 0.75 respectively plotted against blade angle $\theta$ at a fixed upstream rotor thrust. These radial positions were chosen to be at the centre of the tip vortex. Two distinct tip vortex signatures are clearly observed for the cases of $z/D$=0.15 and 0.25. However, at the largest separation distances $z/D$=0.5 the velocity profiles due to two tip vortices can be observed to merge. The reason behind the increase in noise at 0.5 BPF sub-harmonics is likely to be due to this merging of the two tip vortices, which can be clearly seen to differ due to small blade-to-blade differences. In this case, therefore, the mean velocity profile only repeats every one rotation of the rotor leading to tones at 0.5BPF. The reason for the presence of tones at 0.25BPF, implying periodicity at every two rotations of the rotor is currently not understood for $z/D > 0.25$.

To demonstrate explicitly the reasons for the increase in low frequency noise associated with increasing rotor separation distance, the PSD of unsteady velocity shown in figure 10 is plotted again in figure 12 for the three representative separation distances $z/D$ of 0.25, 0.5 and 0.8, against frequency normalised by

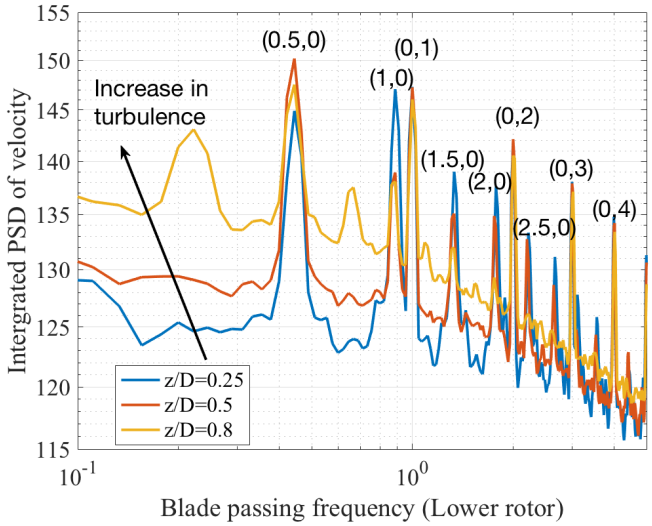


Figure 12: PSD of unsteady velocity integrated over radius weighted by $U^3$ on the downstream rotor plotted against frequency at three different separation distances of $z/D$ =0.25, 0.5 and 0.8 at a fixed combined thrust of 10 N.

the BPF of the downstream rotor. The PSD level at the sub-harmonic frequencies of (0.25,0) and (0.5,0) and low frequency broadband velocity can be observed to increase by more than 10dB as the separation distance $z/D$ is increased from 0.25 to 0.8.

The most likely explanation for this increase is that the tip vortex grows in size as it evolves along the helical path towards the downstream rotor, as indicated in the unsteady velocity color maps of figure 8b. The growth of the tip vortex results in increasing eddy length-scales and hence an increase in low frequency turbulence velocity. The increase in unsteady velocity at these very low frequencies in figure 12 is important for overall noise since this low frequency turbulence energy will be scattered by the downstream rotor into much higher frequencies according to the classical frequency scattering rule reviewed in the next section.

## 6. The basic kinematics of rotor-rotor interaction noise

In this section we present the basic kinematic principles by which the unsteady velocity from the upstream rotor due to the tip and wake interacts with the downstream rotor to produce far field noise. Our objective here is to understand the relationship between the unsteady velocity spectrum versus $z/D$ measured in the stationary reference frame shown in figure 10 to the far field acoustic pressure spectrum versus $z/D$ plotted in figure 6.

For a contra-rotating rotor system, interpretation of aerodynamic and acoustic data due to interaction noise is made difficult since the main source of turbu-

lence is generated in the reference frame rotating with the upstream rotor while the unsteady blade loading, and hence noise radiation, occurs in the reference frame rotating with the downstream rotor. To compound the difficulty, aerodynamic flow measurements are often constrained to be in the stationary reference frame. A framework is therefore needed to understand the relationship between them.

Here, we summarise the essential scattering relationships associated with rotor-rotor turbulence interaction noise in order to establish the relationship between the velocity spectrum from the upstream rotor to the noise radiated by the downstream rotor. In the following derivation we have retained only the essential scattering effects in the direction of rotation. Moreover, in the simple analysis we have assumed harmonic sound fields even though, as we shall show, a dominant part of the noise spectrum is broadband and stochastic in nature. A more complete analysis of the broadband noise due to the interaction between the turbulence from an upstream rotor with a downstream rotor in a Contra-Rotating Open Rotor (CROR) can be found in Ref. [16, 47].

Consider two rotors rotating in the opposite directions. The upstream and downstream rotors are assume to comprise $B^+$ and $B^-$ blades and rotate with angular speed $\Omega^+$ and $-\Omega^-$ respectively ($\Omega^+, \Omega^- > 0$). In the reference frame rotating with the upstream rotor, $\tilde{\mathbf{x}}^+ = \tilde{\mathbf{x}}^+(r, z, \tilde{\theta}^+)$, where $\tilde{\theta}^+ = \theta - \Omega^+\tau$, the unsteady velocity $\mathbf{u}(\tilde{\mathbf{x}}^+)$ due to the upstream rotor may be expressed as the sum of a mean deterministic part $\overline{\mathbf{U}}(\tilde{\mathbf{x}}^+)$ that upon interaction with the downstream rotor produces the tones and a random component $\mathbf{u}_\sigma(\tilde{\mathbf{x}}^+)$ that is responsible for generating broadband noise,

$$\mathbf{u}(\tilde{\mathbf{x}}^+) = \overline{\mathbf{U}}(\tilde{\mathbf{x}}^+) + \mathbf{u}_\sigma(\tilde{\mathbf{x}}^+) \tag{7}$$

In Eq. 7 $\overline{\mathbf{U}}(\tilde{\mathbf{x}}^+)$ is the mean velocity variation obtained after averaging over a large number of blade rotations, while the random component of velocity $\mathbf{u}_\sigma(\tilde{\mathbf{x}}^+)$ is assumed to be of the form,

$$\mathbf{u}_\sigma(\tilde{\mathbf{x}}^+) = \sigma_{\mathbf{u}}(\tilde{\mathbf{x}}^+) n(\tilde{\mathbf{x}}^+) \tag{8}$$

where $n(\tilde{\mathbf{x}}^+)$ is a spatially varying random function has the same single-point and two-point spatial statistics as the turbulent field but with zero mean and unit standard deviation and $\sigma_u(\tilde{\mathbf{x}}^+)$ is the standard deviation of the velocity obtained after averaging over a large number of blade rotations.

The absence of time $\tau$ in Eq. 7 is the result of making the usual assumption of frozen turbulence in which the turbulence velocity in the reference frame moving with the mean flow appears unchanging with time.

*Broadband Sound field*

We consider first the noise generated by the random component

$$\mathbf{u}_\sigma(\tilde{\mathbf{x}}^+) = \sum_m \mathbf{u}_{\sigma,\mathbf{m}}(r, z) e^{\mathrm{j}mB^+\tilde{\theta}^+} \tag{9}$$

so that Eq. (8) becomes,

$$\mathbf{u}_\sigma(\tilde{\mathbf{x}}^+) = \sum_m \sigma_{\mathbf{u},\mathbf{m}}(r,z) n(\tilde{\mathbf{x}}^+) e^{\mathrm{j}mB^+\tilde{\theta}^+} \tag{10}$$

The velocity field $\mathbf{u}_\sigma(\tilde{\mathbf{x}}^-,\tau)$ in the reference frame rotating with the downstream rotor, where interaction noise is generated, may be obtained by putting, $\tilde{\theta}^- = \tilde{\theta}^+ - (\Omega^+ + \Omega^-)\tau$ in Eq. (10), and is of the form,

$$\mathbf{u}_\sigma(r,z,\tilde{\theta^-} - (\Omega^+ + \Omega^-)\tau) = \sum_m \sigma_{\mathbf{u},\mathbf{m}}(r,z) n(r,z,\tilde{\theta^-} + (\Omega^+ + \Omega^-)\tau)) e^{\mathrm{j}mB^+\tilde{\theta}^- + \mathrm{j}mB^+(\Omega^+ + \Omega^-)\tau} \tag{11}$$

Note that at any moment in time, the turbulence field $n$ must be $2\pi$ periodic and hence we can write the circumferential variation of turbulence in terms of Fourier components $n_q(r,z,\tau)$

$$n(r,z,\tilde{\theta^-} + (\Omega^+ + \Omega^-)\tau)) = \sum_q n_q(r,z,\tau) e^{\mathrm{j}q(\tilde{\theta}^- + (\Omega^+ + \Omega^-)\tau)} \tag{12}$$

which is the $\mathrm{q}^{th}$ harmonic of turbulence in the rotating reference frame. The turbulence field in the rotating reference frame of the downstream rotor is therefore of the form,

$$\mathbf{u}_\sigma(\tilde{\mathbf{x}}^-,t) = \sum_m \sum_q \sigma_{\mathbf{u},\mathbf{m}}(r,z) n_q(r,z,\tau) e^{\mathrm{j}\left(mB^+ + q\right)\tilde{\theta}^- + \mathrm{j}\left(mB^+ + q\right)(\Omega^+ + \Omega^-)\tau} \tag{13}$$

This velocity expressed in the downstream rotor reference frame upon interaction with the downstream rotor will induce a pressure jump across a reference blade $\Delta p^{(0)}$ with identical $\tilde{\theta}^-$ and $\tau$ dependence of the form,

$$\Delta p^{(0)}(\tilde{\mathbf{x}}^-,\tau) = \sum_m \sum_q \Delta p^{(0)}_{mq}(r,z,\tau) e^{\mathrm{j}\left(mB^+ + q\right)\tilde{\theta}^- + \mathrm{j}\left(mB^+ + q\right)(\Omega^+ + \Omega^-)\tau} \tag{14}$$

where $\Delta p^{(0)}_{mq}(r,z,\tau)$ is the $(m,q)^{\mathrm{th}}$ component of pressure jump due to $(\mathrm{m},\mathrm{q})^{th}$ component of upwash velocity of the form $\sigma_{\mathbf{u},\mathbf{m}}(r,z) n_q(r,z,\tau)$. For $B^-$ identical blades the pressure jump repeats at angular intervals of $2\pi/B^-$ and hence the pressure jump including all blades is of the form

$$\Delta p(\tilde{\mathbf{x}}^-,\tau) = \frac{B^-}{2\pi} \sum_m \sum_n \sum_q \Delta p^{(0)}_{mq}(r,z,\tau) e^{\mathrm{j}\left(mB^+ + q\right)\tilde{\theta}^- + \mathrm{j}\left(mB^+ + q\right)(\Omega^+ + \Omega^-)\tau + \mathrm{j}nB^-\tilde{\theta}^-} \tag{15}$$

Calculation of the radiated noise requires the time and space variation of the unsteady force $\Delta p(\mathbf{x},\tau)$ acting on the fluid in the stationary reference frame,

which obtained from Eq. (15) by putting $\theta = \tilde{\theta}^- + \Omega^+\tau$. Collecting terms the unsteady blade loading responsible for sound radiation is of the form,

$$\Delta p(\mathbf{x},\tau) = \frac{B^-}{2\pi}\sum_m\sum_n\sum_q \Delta p^{(0)}_{mq}(r,z,\tau)e^{\mathrm{j}\omega_{qmn}\tau+\mathrm{j}l\theta} \tag{16}$$

where

$$\omega_{qmn} = \left(q + mB^+\right)\Omega^- - nB^-\Omega^+ \tag{17}$$

and

$$l = q + mB^+ + nB^- \tag{18}$$

*Tonal sound field*

Assuming $B^+$ identical blades, the mean velocity variation $U(\tilde{x}^+)$ may be expressed as the Fourier series,

$$\mathbf{U}(\tilde{\mathbf{x}}^+) = \sum_m \mathbf{U_m}(r,z)e^{\mathrm{j}mB^+\tilde{\theta^+}} \tag{19}$$

The form of the unsteady pressure due to the mean velocity profile $\mathbf{U}(\tilde{\mathbf{x}}^+)$ then follows exactly the same procedure as for the random component $\mathbf{u}_\sigma(\tilde{\mathbf{x}}^+)$, leading to the same final expression for $\Delta p(\mathbf{x},\tau)$ of Eq. (16) and the identical scattering rules of Eqs. (17) and (18) with the important difference that the scattering index q associated with the turbulence velocity with $2\pi$ periodicity is zero, $q = 0$ ([48, 36, 2]).

Having established the form of $\Delta p(\mathbf{x},\tau)$ the far field radiated pressure can be calculated from classical rotor theory. Summing over the radiation 0 to $B^-$ blades the radiated acoustic pressure at any observer time $t$ can be obtained from,.

$$\mathbf{p}(\mathbf{x},t) = \frac{1}{4\pi c_0}\int \sum_{k=1}^{B^-}\frac{\partial}{\partial t}\left(\frac{\Delta p^k(\tilde{\mathbf{x}}^-,t)\mathbf{n}.\mathbf{r}}{R(1-M_R)}\right)_{\tau=t-R/c} dS \tag{20}$$

where $\mathbf{n}$ is the unit vector normal to the blade and $\mathbf{r}$ is the vector between the source and receiver point at emission time $\tau$ and $R = |r|$. Equation (20) may be evaluated in terms of standard functions for far field observers [48, 36, 2]. Note that an additional complication for the prediction of the broadband noise is that $\Delta p^k(\tilde{\mathbf{x}}^-,t)$ is a stochastic quantity and hence the two-point turbulence velocity statistics $E[n(\tilde{\mathbf{x}^+})n(\tilde{\mathbf{x}^+} + \Delta\tilde{\mathbf{x}^+})]$ must be determined.

*Frequency Scattering*

The frequency scattering rule of Eq. (17), $\omega_{qmn} = (q + mB^+)\,\Omega^- - nB^-\Omega^+$, highlights the complication with relating the rotor wake turbulence generated in the rotating reference frame of the upstream rotor to its subsequent noise generation by the downstream rotor rotating in the opposite direction.

$$\Delta p(\mathbf{x},\omega) = \frac{B^-}{2\pi}\sum_m\sum_n\sum_q e^{\mathrm{j}l\theta}\int_{-\infty}^{\infty}\Delta p^{(0)}_{mq}(r,z,\tau)e^{\mathrm{j}(-\omega+\omega_{qmn})\tau}d\tau \tag{21}$$

$$\Delta p(\mathbf{x},\omega) = \frac{B^-}{2\pi}\sum_m\sum_n\sum_q e^{\mathrm{j}l\theta}\Delta p^{(0)}_{mq}(r,z,\omega - \left(q + mB^+\right)\Omega^- + nB^-\Omega^+) \tag{22}$$

This analysis highlights the difficulty in interpreting aerodynamic and acoustic data for a contra-rotating rotor system since the main source of turbulence is generated in the reference frame rotating with the upstream rotor while the unsteady blade loading, and hence noise radiation, occurs in the reference frame rotating with the downstream rotor. To compound the difficulty, aerodynamic flow measurements are often constrained to be in the stationary reference frame. A framework is therefore needed to understand the relationship between them.

## 7. Role of tip vortex interactions on Broadband noise: $z/D > z_0/D$

The effects of frequency scattering of the turbulence velocity on noise, summarised by Eq. (17), can be clearly seen in figures 13a and b which show the PSD difference in dB due to both hot-wire velocity data and the far-field noise data respectively relative to their spectra at the optimum separation distance $z_0/D = 0.25$. Results are given for the three values of $z/D$ of 0.5, 0.8 and 1. The velocity spectra in Figure 13a were computed by integrating the unsteady velocity spectra measured across the blade radius, with tones removed, and weighted by $U^3(r)$ as indicated above.

The maximum noise increase relative to the optimum noise at $z_0/D = 0.25$ in Figure 13b can be observed at $5^{th}$ BPF, where increases by about 5 dB, 11 dB and 14 dB are obtained at the three separation distances. Almost the same increase in acoustically-weighted turbulence velocity spectra can be observed in Figure 13a but at the much lower frequencies, below 0.5BPF, where the turbulence velocity spectrum is largest (figure 10), Therefore, the increase in noise at the peak frequency arises from scattering of the low frequency turbulence velocity into much higher frequencies. We note that both the noise and turbulence velocity spectra are close to 0 dB at much higher frequencies, suggesting that frequency scattering effects are likely to be less important in this high frequency range. This is because frequency scattering occurs at integer multiples of $\Omega^+$ (Eqs (17) and (18)), which is relative small at high frequencies but is significant at much lower frequencies. In general, however, there is no simple relationship

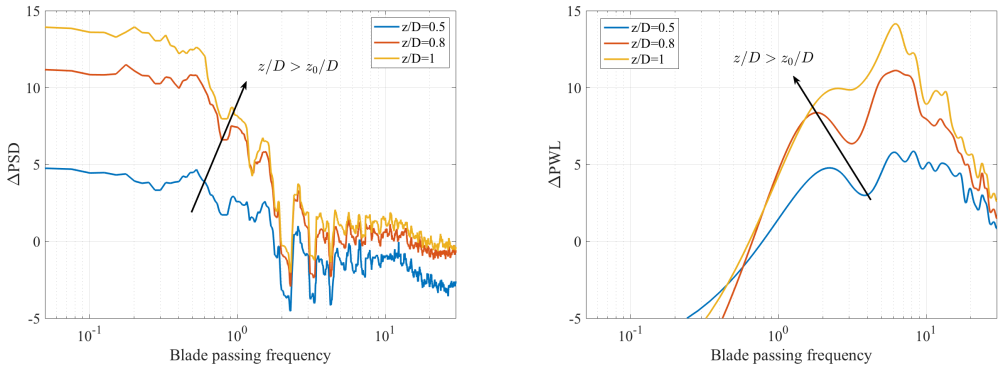


Figure 13: Change in Integrated PSD of upwash velocity with $U^3$ scaling (left), sound power level for broadband component (right) over radius on the downstream rotor plotted against frequency at three different separation distances of $z/D$ =0.5, 0.8 and 1 at a fixed combined thrust of 10 N.

between the velocity spectrum due to the upstream rotor and the subsequent far field noise spectrum.

A similar principle also exists to explain the increase in 'tonal' amplitudes observed in Figure 7, which we discuss below.

## 8. Influence of separation distance on tonal noise

### *8.1. Role of potential field interactions: $z/D < z_0/D$*

The amplitude of the tones at the even-harmonic frequencies can be seen to be significantly greater than those of the odd-harmonics at small separation distances. Moreover, their amplitudes can be seen to decay with increasing $z/D$ unlike those of the odd harmonics, which appear insensitive to separation distance. These dominant even-harmonic interaction tones will be shown in the next figure to decay exponentially with increasing $z/D$, which is the characteristic of potential field decay [48]. This behaviour is therefore strongly indicative of noise arising from the interaction between the potential field of each rotor with the neighbouring rotor. The classical frequency scattering rule $\omega_{mn} = mB^+\Omega^+ + nB^-\Omega^-$ suggests that all tonal frequencies due to interaction must occur at the even harmonics since $\Omega^+ \approx \Omega^-$ and $B^+ = B^-$. The tonal amplitudes at the odd harmonic frequencies must therefore be due to rotor alone sources, which explains their insensitivity to separation distance.

To investigate in greater detail the decay of the interaction tones at the even-harmonic frequencies, based on an assumed dependence of $e^{-\beta nz/D}$, where $\beta$ is a constant, the overall total noise is plotted against $nz/D$ in figure 14 for the $2^{\text{nd}}$, $4^{\text{th}}$, $6^{\text{th}}$ and $8^{\text{th}}$ harmonics, where $n$ is the harmonic frequency. Plotted against $nz/D$, the overall sound power level exhibits a close approximation to straight line decay for separation distance $nz/D < 1$, suggesting that that the pressure amplitude due to potential field interactions is proportional to $e^{-\beta nz/D}$, where

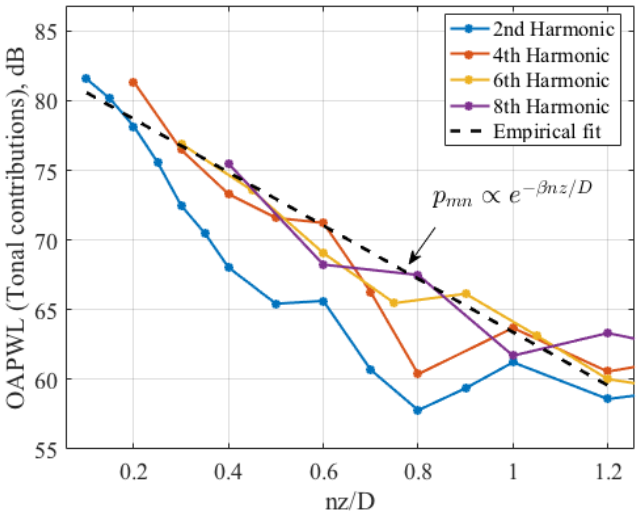


Figure 14: Overall sound power levels for 2nd, 4th, 6th and 8th harmonic tones plotted against non-dimensional distance $z/D$ and blade passing frequency at a fixed combined thrust of 16 N.

$\beta$=2.2. This finding is consistent with the formulations developed in the PhD thesis of [48]. The noise due to the higher harmonic frequencies therefore has a higher rate of decay as clearly observed in figure 6. This hypothesis is further validated by a simple analytical model proposed in section 8.3.

### *8.2. Role of tip vortex interactions on 'Tonal' noise: $z/D > z_0/D$*

#### *8.2.1. Mean flow characteristics*

Pure tones (as distinct from the pseudo tones discussed in section 8.2.2) are radiated by the downstream rotor due to its interaction with the periodically varying mean flow arising from the tip vortex and wake from the upstream rotor.

Figure 15 shows the ensemble-average velocity due to the upstream rotor wake plotted against blade angular position for the three values of $z/D$= 0.15, 0.25 and 0.5. The radial position of the hot wire measurement for the three cases was adjusted to $r/R$ =0.8, 0.75 and 0.75 in order to track the trajectory of the tip vortex. Also shown in this figure is the mean flow behaviour at ($z/D$, $r/R$)=(0.25,0.5) which corresponds to a location where the mean wake velocity profile is dominant at the optimum separation distance. From this figure we can make the following key observations:

1. For the two smallest values of $z/D = 0.15, 0.25$, the tip vortex flow from each blade is distinct and almost identical. At the largest separation distance $z/D = 0.5$ the tip vortices from each blade are observed to merge and exhibit larger difference. At large $z/D$ therefore, the mean flow repeats only once every rotation resulting in tonal noise generation at 0.5BPF.

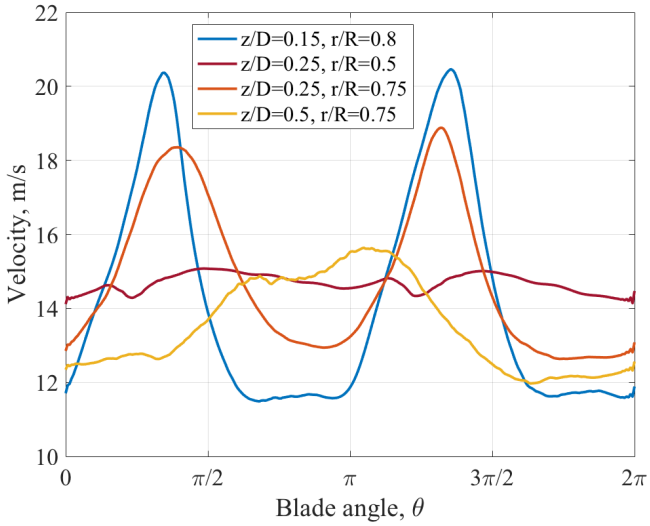


Figure 15: Wake profiles at three different separation distances of $z/D$ =0.15, 0.25 and 0.5 at a fixed upstream rotor thrust.

Precisely this behaviour can be observed in figure 10 for the variation of the velocity spectrum versus $z/D$ in which strong 0.5BPF tones only appear for $z/D > 0.3$.

2. The mean wake from the rotor measured in-board of the tip, whose velocity is about one half of the maximum velocity at the tip, can be seen to vary very little over one rotation, suggesting that tonal amplitudes generated from the flow in this region are comparatively small. It is likely, therefore, that the wake is extremely weak and may be disregarded as an important source of tonal noise.
3. The tip vortex moves rapidly in board as it propagates downwards due to the Vena Contracta effect and grows in size. The tip vortex appears to dissipate rapidly by $z/D \approx 0.5$.

*8.2.2. Tip-vortex empirical model*

Figure 9 has indicated the presence of a strong tip vortex that grows in size as it convects with the mean flow before dissipating. The variation of noise due to tip vortex interaction with $z/D$ will therefore depend on the rate of growth of the tip vortex strength with distance. Majjigi et al. [45] has derived an empirical expression for the tip vortex circulation as a function of the helical path length normalised on the blade chord $(z^+ - z^-)/\cos(\alpha^+)$, where $\alpha^+$ is the blade stagger angle at the tip of the upstream rotor. The expression was originally expressed in terms of the vortex circulation and core size, both of which were linked to the lift coefficient at the tip. The final empirical expression for the circulation as a function of streamwise distance was derived by curve fitting through the

measured vortex circulation downstream of a finite span NACA0012 aerofoil at various angles of incidence and flow speeds. Predictions of the tip vortex circulation allow calculation of the upwash velocity $u$ onto the downstream rotor, which following classical unsteady lift theory [44], can be used to predict the unsteady loading $\Delta p$ on the blade. Following this procedure, the variation in unsteady pressure jump across the downstream blade due to the tip vortex interaction versus helical path length distance $z_h$ can be expressed in terms of upwash velocity as,

$$u \propto \frac{0.01584(z_h/c) + 0.0014}{0.184(z_h/c) + 1} \left[ \frac{1}{(1 + z_h/c)^{\eta}} \frac{0.024(z_h/c) + 0.5586}{0.0504(z_h/c) + 1} \right]^3 \tag{23}$$

where $\eta$ is an empirical constant that depends on whether the rotor is ducted ($\eta$= 1/2) or unducted ($\eta$= 0).

Upon arriving at the downstream rotor with axial velocity $U_z$ the large-scale tip vortex of size $\Lambda$ will be periodically 'chopped' for a duration $L/U_z$. The downstream rotor will therefore respond periodically for this duration resulting in a number of narrow band peaks in the frequency spectrum with a frequency bandwidth of $U_z/\Lambda$. These 'tonal' components are often referred to as pseudo-tones as a result of their non-zero frequency bandwidth. This phenomenon was first described by Ref.[6] in a study of rotor noise due to turbulence ingestion. In the present example the frequency bandwidth is approximately 50 Hz based on an estimate of $\Lambda$=0.033 m from hot-wire data and $U_z$=10.5 m/s from figure 8.

*8.3. Breakdown of tonal interaction noise sources*

Section 8.2.2 has highlighted the role of potential field interactions on tonal noise at $z/D < z_0/D$ and section 8.2.1 has revealed the role of tip vortex interactions on tonal noise at $z/D > z_0/D$. Another contributor to tonal noise arises from the periodic wake interaction from the upstream rotor with the downstream rotor [48].

In this section we compare the variation of the noise versus rotor separation distance due to these three source contributions against published semi-empirical expressions.

The upwash velocity $u$ on a downstream blade incident on the downstream blade row can be expressed as an infinite series of wake profiles, each of which is of the form [48],

$$u \propto (z/c - 0.5)^{-0.5} \left[ e^{-\frac{k}{z/c - 0.5}} \right] \tag{24}$$

where $k$ is an empirical constant which is a function of drag coefficient $C_D$ and chord length $c$.

For the case of potential field interactions, following the work of [48], the upwash velocity on a downstream blade due to potential field interactions from an upstream blade is given by,

$$u \propto e^{-\frac{k_n B}{r}(z - \frac{c}{2} e^{\mathrm{i}\alpha_d}) + \mathrm{i}(\alpha_d - \alpha_u)}, \tag{25}$$

where $k_n$ is the harmonic, $\alpha_u$ and $\alpha_d$ are the pitch of upstream and downstream rotors respectively. It is clear from Equation (25) that the contribution of the potential field depends on the pitch angles of individual rotors. However, as observed previously by [23], the aerodynamic optimum separation distance is a function of the relative pitch angles between the two rotors. More work is required to identify the influence of pitch angles on the optimum separation distance for noise.

We now use the relationships between unsteady upwash velocity on the rotor and separation distance obtained from Eqs (23), (24) and (25) to predict the overall radiated sound power level by using $20\log_{10}(u)+constant$. The constant is chooses such that the peak sound power level matches with the prediction. The following assumptions are made in the predictions:

1. The first 5 dominant harmonics of the potential field interactions are considered and the amplitude of each harmonic is assumed to be identical.
2. Both the upstream and downstream rotors are identical and their respectively blade angles are same i.e. $\alpha_d = \alpha_u$.
3. The chord is assumed to be constant along the span and equal to its value at $r/R$=0.75.
4. The predicted variation in overall noise versus $z$ for each source is adjusted to match the experimental noise level at $z/D$=0 and $z/D$=1 since only the variation with $z$ is of interest here.

Figure 16 shows the comparison between measured and predicted overall sound power level for tonal noise plotted against separation distance $z/D$ at a fixed combined thrust of 16N. Three predictions for individual noise sources and the overall noise predictions are plotted in figure 16. Very good agreement is observed in the general trends, demonstrating that at the optimum separation distance of $z/D \approx 0.25$ all interaction noise sources contribute almost equally to the overall noise. The level of agreement is sufficiently close to provide confidence in the proposed source balance.

## 9. Influence of diameter mismatch on radiated noise

The value of the optimum separation distance of $z_0/D_u = 0.25$ identified in figure 5 is now investigated for different combinations of upstream and downstream rotor diameter $D_u$ and $D_l$ respectively.

This study will also illustrate that the enhancedd tip vortex interactions are both broadband and tonal as discussed previously in sections 7 and 8.2.

Figure 17 is a plot of the overall sound power level versus separation distance $z/D_u$ for the two cases of $(D_u, D_l)$= (18",18") and (18",16"). The comparison was made at the the same combined thrust of 16 N obtained by the adjusting the RPM of the downstream rotor. Also shown is the predicted variation in overall sound power levels for the tip vortex interaction noise based on the semi-empirical model of the tip vortex velocity of Eq. (23). The RPM of the

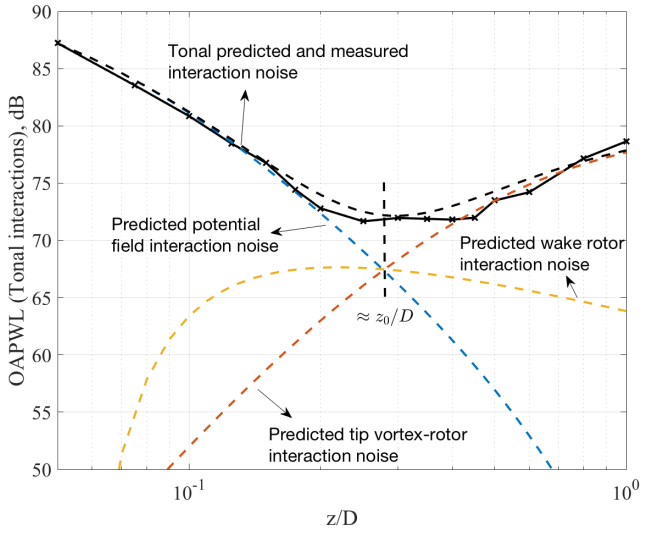


Figure 16: Comparison between measured and predicted overall sound power levels for tonal interaction noise source with separation distance $z/D$ at combined thrust of 16 N.

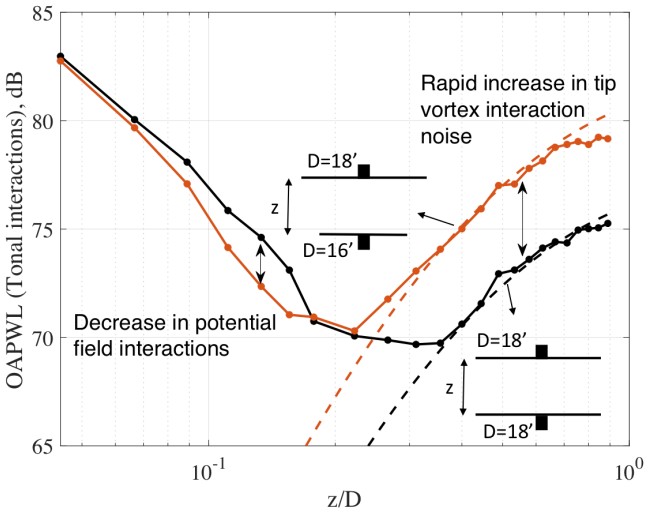


Figure 17: Overall sound power level of net tonal interaction contribution variation with separation distance for different diameter combinations at a fixed combined thrust of 16N

upstream rotor remained fixed at $\approx$ 3011 while the RPM of the 18" and 16" diameter downstream rotors was 3201 and 4097 respectively.

The absolute predicted tip vortex noise levels for both rotor configurations was adjusted to fit the experimental data by adding to $20\log_{10}(u)$ of Eq. (23) a single common offset of 160 dB. The noise predictions for the (18",16") configuration includes an additional factor of $30\log_{10}(U_{l_16}/U_{l_18})$, where $U_l$ is the relative velocity of the tip vortex interactions with the downstream rotor, $U_l = \Omega_1 R_1 + \Omega_2 R_2$, where $R_1$ is the radial position at which the tip vortex interacts with the downstream rotor, obtained from hot wire measurement. This velocity correction factor was included to take into account the $U_l^3$ velocity scaling for leading edge interaction noise [44].

Figure 17 clearly indicates the validity of the semi-empirical expression of Eq. (23) for the tip vortex velocity and the $U_l^3$ velocity scaling to account for the increase in noise due to the increase in velocity of the downstream rotor necessary to maintain constant thrust. Moreover, it highlights the dominance of the tip vortex at rotor separation distances greater than the optimum distance $z_0$.

In this figure the optimum separation distance $z_0/D$ is observed to reduce as the RPM of the smaller downstream rotor is increased to maintain constant thrust. This is due to a reduction in the potential field and an increase in the tip vortex interaction noise. Secondly, reducing the diameter of the downstream rotor (cropping) does not necessarily lead to a reduction in the overall noise, as reported in some studies [34] but depends on the position of the tip vortex interaction with the downstream rotor and the operating conditions.

Finally, we compare in Figure 18a the sound power spectra at the separation distances below and equal to the optimum distance, $z/D$ =0.044 and 0.22, while Figure 18b is a comparison of the spectra at above and equal to the optimum separation distances, $z/D$ =0.22 and 0.75 respectively, for the (18",16") configuration at a fixed thrust of 16N. As both rotors are rotating at different RPM their blade passing frequencies now differ allowing the contributions from the individual rotors to be identified. These rotor-alone tones are additional to the interaction tonal frequencies leading to a more complex spectrum than when their RPM's are identical.

Figure 18a clearly demonstrate that at the separation distance smaller than the optimum distance, $z/D < 0.22$, interaction tones are dominant while the broadband noise at both the separation distances are almost identical. By contrast, in Figure 18b, significant increases in both tonal and broadband noise is observed at the larger separation distances $z/D > 0.22$. An important finding in Figure 18b is that this increase in tonal noise only occurs at the harmonic frequencies of the downstream rotor, which provides direct evidence of an increase in the strength of the tip vortex. This phenomenon has been previously observed by [49, 6].

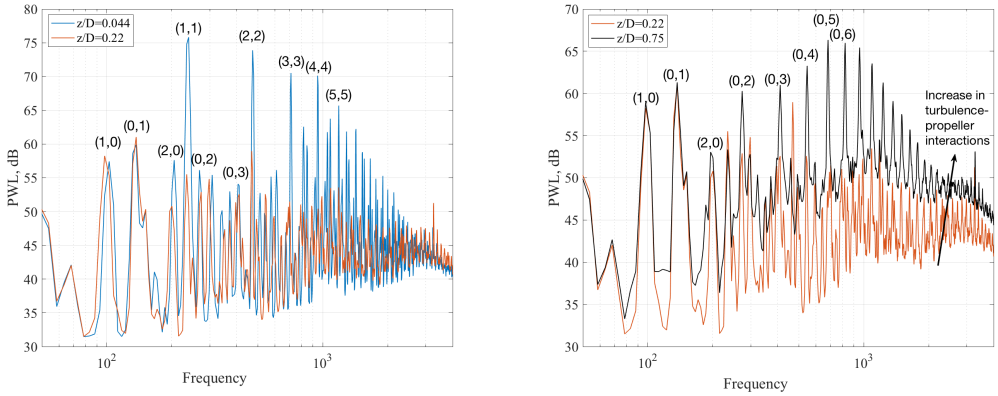


Figure 18: Sound power level plotted against frequency for three separation distances of $z/D$ =0.044, 0.22 and 0.75 for (18",16") configuration at fixed combined thrust of 16 N.

## 10. Aerodynamics performance

Finally in this section the aerodynamic performance of the (16",16") contra-rotating rotor is investigated. The total electric power to the rotor rig and its total thrust was determined in order to compute the aerodynamic efficiency. Figure 19 shows the efficiency in grams per watts versus overall sound power level at various separation distances $z/D$ between 0.05 to 1 at a fixed combined thrust of 10N.

A well defined optimum separation distance for minimum noise can be observed at about $z/D = 0.25$. At this distance the efficiency is 7.32 g/W, which is only 5% less than of the maximum efficiency of 7.36 g/W, which occurs at about $z/D = 0.5$, where noise levels are about 1dB higher. Clearly, therefore, any separation distance within $0.25 < z/D < 0.5$ provides a good balance between aerodynamic efficiency and low noise. The optimum separation distance of $z/D = 0.25$ for aerodynamic performance was identified in previous work by Refs. [23, 25], attributed to the merging of both the wake trajectories of the upstream and downstream rotors. The authors demonstrated that the upwash effect of the contracted upstream rotor wake on the downstream rotor plays a fundamental role in improving the hover performance of contra-rotating rotors.

Figure 20 shows color maps of overall sound power level plotted against separation distance $z/D$ and aerodynamic efficiency for varying total thrust between 2 and 20N. Also shown on this figure as a line graph are the variations in efficiency versus $z/D$. Color maps of the variation in noise (normalized by $10\log(t^{2.75})$) versus efficiency and $z/D$ are also shown in Fig 20 at the varying thrust settings, whilst maintaining zero net torque. The separation distances of low noise and maximum efficiency are clearly delineated in the range $0.25 < z/D < 0.5$, whereby by changing the separation distance has relatively little affect on noise and efficiency.

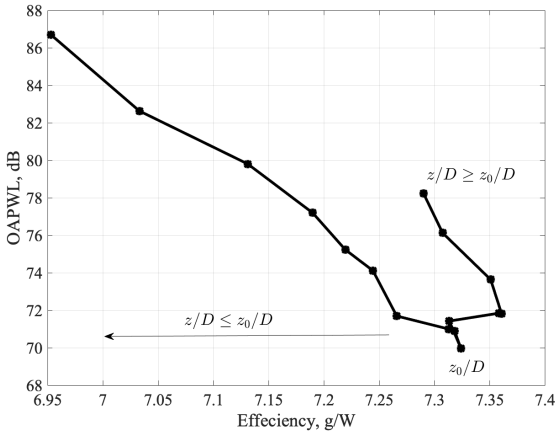


Figure 19: Efficiency vs. sound power level for various non-dimensional separation distances $z/D$ at a fixed combined thrust of 10 N.

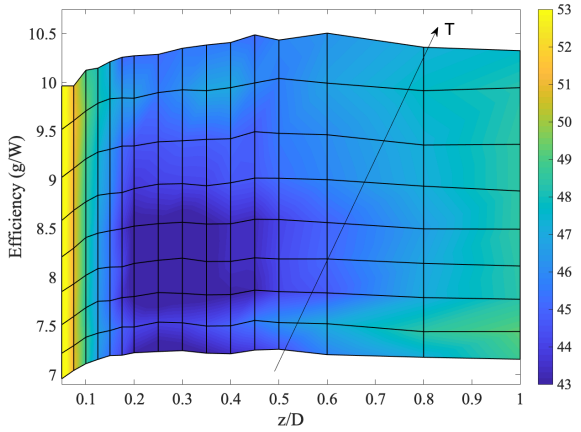


Figure 20: Efficiency vs. sound power level (normalized on $10\log(t^{2.75})$) for various non-dimensional separation distances $z/D$ for combined thrust conditions varying from 2 N to 20 N.

## 11. Conclusion

This paper has investigated experimentally the influence of separation distance on radiated noise in co-axial contra-rotating rotors. Based on measurements of the overall sound power level for a range of rotor thrusts and diameters, this paper has identified separation distances approximately in the range $0.25 < z/D < 0.5$ where the noise radiated is a minimum and the aerodynamic efficiency is high. This range of separation distances has been shown to be attributed an optimum balance between the various dominant sources. The potential field interactions are shown to dominate overall noise at separation distances smaller than the optimum distance, $z/D < z_0/D$, while the noise due to tip vortex interaction is dominant for distances greater than the optimum value, $z/D > z_0/D$. A simple semi-empirical framework has been proposed to validate this hypothesis. Very good agreements are observed in the general trends, demonstrating that at the optimum separation distance of $z/D \approx 0.25$ all interaction noise sources contribute almost equally to the overall noise. The simple scaling law, $N^{5.5}D^7$, has also been found to describe the measured variation in total radiated sound power versus the rotor RPM $N$ and the rotor diameter $D$.

In typical drone contra-rotating drone architectures, we usually have a single boom in between the two rotors. However, the conclusion of the study doesn't change as the noise generating sources Rotor wake-boom interaction, boom wake-rotor interaction will be similar for both the configurations. In conclusion, this present study will help to design the contra-rotating co-axial rotorrotor system for low noise. Future work involves, investigating the optimum separation distance for various combinations of rotor diameters and number of blades for co-axial contra-rotating rotors and also looking at non-co-axial rotor systems.


## Acknowledgments

The first author would like to acknowledge the financial support of the Royal Academy of Engineering, United Kingdom (RF/201819/18/194). The authors would also like to thanks Dr. Mantas Brazinskas for his efforts in building this rig during his PhD studies. The authors would like to thank funders for the financial support from the EPSRC Research Grant No: EP/N010523/1 for supported the development of the test-rig.


## References


[1] C. P. Coleman, Uk expert report on drones, Pwc report (2018).

[2] D. B. Hanson, Helicoidal surface theory for harmonic noise of propellers in the far field, AIAA Journal 18(10) (1980) 1213–1220.

[3] F. Farassat, Linear acoustic formulas for calculation of rotating blade noise, AIAA Journal 19(9) (1981) 1122–1130.

[4] F. Farassat, Prediction of advanced propeller noise in the time domain, AIAA Journal 24(4) (1986) 578–584.

[5] R. K. Amiet, Noise produced by turbulent flow into a rotor: theory manual for noise calculation, NASA Technical Report NASA CR-181788 (1989).

[6] R. W. Paterson, R. K. Amiet, Noise of a model helicopter rotor due to ingestion of isotropic turbulence, Journal of Sound and Vibration 85(4) (1982) 551–577.

[7] P. Block, Noise radiation patterns of counter-rotation and unsteadily loaded single-rotation propellers, J. Aircraft 22 (1985) 776–783.

[8] D. B. Hanson, Noise of counter-rotation propellers, Journal of Aircraft 22 (1985) 609–617.

[9] B. Magliozzi, P. Brown, D. Parzych, Acoustic test and analysis of a counter-rotating prop-fan model, NASA Technical Memorendum CR-179590 (1987).

[10] A. B. Parry, D. G. Crighton, Asymptotic theory of propeller noise. i - subsonic single-rotation propeller, AIAA Journal 27(9) (1989) 1184–1190.

[11] N. Peake, D. G. Crighton, An asymptotic theory of near-field propeller acoustics, Journal of Fluid Mechanics 232 (1991) 285.

[12] D. G. Crighton, A. B. Parry, Higher approximations in the asymptotic theory of propeller noise, AIAA Journal 30(1) (1992) 23–28.

[13] S. J. Majumdar, N. Peake, Noise generation by the interaction between ingested turbulence and a rotating fan, Journal of Fluid Mechanics 359 (1998) 181–216.

[14] Q. Zhou, P. Joseph, Frequency-domain method for rotor self-noise prediction, AIAA Journal 44(6) (2006) 1197–1206.

[15] M. J. Kingan, R. H. Self, Counter-rotation propeller tip vortex interaction noise, in: 15th AIAA/CEAS Aeroacoustics, 2009.

[16] V. P. Blandeau, P. F. Joseph, Broadband noise due to rotor-wake/rotor interaction in contra-rotating open rotors, AIAA Journal 48(11) (2010) 2674–2686.

[17] M. Roger, A. Carazo, Blade-geometry considerations in analytical gust-airfoil interaction noise models, in: 16th AIAA/CEAS Aeroacoustics Conference, no. AIAA 2010-3799, 2010.

[18] N. Peake, A. B. Parry, Modern challenges facing turbomachinery aeroacoustics, Annual Review of Fluid Mechanics 44(1) (2012) 227–248.

[19] A. B. Parry, S. Vianello, A project study of open rotor noise, International Journal of Aeroacoustics 11(2) (2012) 247–258.

[20] M. J. Kingan, Open rotor broadband interaction noise, Journal of Sound and Vibration 332(17) (2013) 3956–3970.

[21] S. Sinayoko, M. J. Kingan, A. Agarwal, Trailing edge noise theory for rotating blades in uniform flow, Proceedings of the Royal Society A: Mathematical, Physical and Engineering Sciences 469: 20130065 (2013) 1–21.

[22] C. P. Coleman, A survey of theoretical and experimental coaxial rotor aerodynamic research, NASA Technical Memorendum NASA-TP-3675 (1997).

[23] T. Nagashima, K. Nakanishi, Optimum performance and wake geometry of co-axial rotor in hover, Vertica 7 (1983) 225–239.

[24] J. G. Leishman, M. Syal, Figure of merit definition for coaxial rotors, Journal of the American Helicopter Society 53(3) (2008) 290–300.

[25] Y. Lei, Y. Ji, C. Wang, Optimization of aerodynamic performance for coaxial rotors with different rotor spacings, International Journal of Micro Air Vehicles 10(4) (2018) 362–369.

[26] M. Brazinskas, S. D. Prior, J. P. Scanlan, An empirical study of overlapping rotor interference for a small unmanned aircraft propulsion system, Aerospace 3(4) (2016) 32.

[27] M. Ramasamy, Hover performance measurements toward understanding aerodynamic interference in coaxial, tandem, and tilt rotors, Journal of the American Helicopter Society 60(3) (2015) 1–17.

[28] F. Bohorquez, Rotor hover performance and system design of an efficient coaxial rotary wing micro air vehicle, Ph.D. thesis, University of Maryland, USA (March, 2007).

[29] D. Shukla, N. Komerath, Drone scale coaxial rotor aerodynamic interactions investigation, Journal of Fluid Engineering 141(7) (2019) 225–239.

[30] D. Shukla, N. Komerath, Low reynolds number multirotor aerodynamic wake interactions, Experiments in Fluids 60:77.

[31] J. E. F. Williams, Y. P. Guo, Sound generated from the interruption of a steady flow by a supersonically moving aerofoil, Journal of Fluid Mechanics 195 (1988) 113–135.

[32] A. M. Cargill, Tip effects in the interaction of gusts and vortices with a wing at m = 1, Rolls-Royce Theoret. Sci. Group Rep. TSG 0294 (1987).

[33] R. P. Woodward, Noise of a model high speed counterrotation propeller at simulated takeoff/approach conditions, NASA Technical Memorandum N88-70592 (1987).

[34] J. H. Dittmar, The effect of front to rear propeller spacing on the interaction noise of model counter-rotation propeller at cruise, NASA Technical Memorandum NASA TM-100121 (1987).

[35] G. Hoff, Experimental performance and acoustic investigation of modern, counterrotating blade concepts, NASA Contractor Report 185158 (1990).

[36] A. B. Parry, M. Kingan, B. Tester, Relative importance of open rotor tone and broadband noise sources, in: 18th AIAA/CEAS Aeroacoustics Conference, no. AIAA-2012-2307, 2011.

[37] J. H. Dittmar, D. B. Stang, Noise reduction for model counterrotation propeller at cruise by reducing aft-propeller diameter, NASA Technical Memorandum 88936 (1987).

[38] R. S. McKay, M. J. Kingan, R. Go, Experimental investigation of contra-rotating multi-rotor uav propeller noise, in: Proceedings of ACOUSTICS, Cape Schanck, Victoria, Australia, 2019.

[39] K. D. Munz, V. Raghav, Design and development of a small-scale coaxial rotor for aeroacoustic investigation, in: AIAA SciTech Forum, no. AIAA-2020-1497, 2020.

[40] A. J. Torija, P. Chaitanya, Z. Li, Psychoacoustic analysis of contra-rotating propeller noise for unmanned aerial vehicles, The Journal of the Acoustical Society of America 149(2) (2021) 835–846.

[41] J. E. Marte, D. W. Kurtz, A review of aerodynamic noise from propellers, rotors, and lift fans, NASA Technical Report NASA-32-7462 (1970).

[42] N. S. Zawodny, D. D. B. Jr., Investigation of rotor-airframe interaction noise associated with small-scale rotary-wing unmanned aircraft systems, in: AHS 73rd Annual Forum, Fort Worth, Texas, 2017.

[43] W. T. W. Cory, Fans and Ventilation,, Elsevier Science, Paris, 2005.

[44] R. K. Amiet, Noise due to turbulent flow past a trailing edge, Journal of Sound and Vibration 47 (3) (1976) 387–393.

[45] R. K. Majjigi, K. Uenishi, P. R. Gliebe, An investigation of counter-rotating tip vortex interaction, NASA Technical Report NASA-CR-185135 (1989).

[46] R. Amiet, Acoustic radiation from an airfoil in a turbulent stream, Journal of Sound and Vibration 41(4) (1975) 407–420.

[47] V. Blandeau, Aerodynamic broadband noise form contra-rotating open rotors, Ph.D. thesis, University of Southampton (March 2011).

[48] A. B. Parry, Theoretical prediction of counter-rotating propeller noise, Ph.D. thesis, University of Leeds (1988).

[49] R. K. Amiet, Noise produced by turbulent flow into a propeller or helicopter rotor, AIAA Journal 15(3) (1977) 307–308.